




RESEARCH ARTICLE

Inelastic electron scattering by the gas phase in near ambient pressure XPS measurements

Lukas Pielsticker¹  | Rachel Nicholls¹ | Sebastian Beeg¹ | Caroline Hartwig¹ | Gudrun Klihm¹ | Robert Schlögl^{1,3} | Sven Tougaard²  | Mark Greiner¹ 

¹Department of Heterogeneous Reactions, Max Plank Institute for Chemical Energy Conversion, Mülheim an der Ruhr, Germany

²Department of Physics, Chemistry and Pharmacy, University of Southern Denmark, Odense, Denmark

³Department of Inorganic Chemistry, Fritz-Haber Institute of the Max-Planck Society, Berlin, Germany

Correspondence

Mark Greiner, Department of Heterogeneous Reactions, Max Plank Institute for Chemical Energy Conversion, Mülheim an der Ruhr, Germany.

Email: mark.greiner@cec.mpg.de

Funding information

Max-Planck-Gesellschaft

X-ray photoemission spectroscopy (XPS) measurements in near-ambient pressure (NAP) conditions result in a signal loss of the primary spectrum as a result of inelastic scattering of photoelectrons in the gas phase. The inelastic scattering of the primary electrons gives rise to a secondary signal that can result in additional and often unwanted features in the measured spectrum. In the present work, we derive equations that can be used to model the resulting signal and provide equations that can be used to simulate or remove the inelastic scattering signal from measured spectra. We demonstrate this process for photoemission spectra of a wide range of kinetic energies, measured from Au, Ag, and Cu, in a variety of gases (N₂, He, H₂, and O₂). The work is supplemented with an open-source software in which the algorithms described here have been implemented and can be used to remove the gas phase inelastic scattering signal.

KEYWORDS

electron spectroscopy, inelastic scattering, in situ

1 | INTRODUCTION

In recent years, the use of near-ambient pressure XPS (NAP-XPS) has steadily increased its popularity for research in materials, catalysis, electrochemistry, corrosion, and biomaterials.^{1–13} In a NAP-XPS measurement, a photoemission signal is measured from a sample, while the sample is exposed to a gas atmosphere. Pressures for NAP-XPS measurements typically range from 0.01 up to 100 mbar.

The measured photoelectrons must travel from the sample surface to a photoelectron detector (i.e., through an electrostatic lens system and a hemispherical analyzer, to an electron amplifier and detector), as illustrated in Figure 1. Before the electrons reach the entrance slit of the photoelectron spectrometer, they travel a certain distance (approximately 0.1–1 mm) through a relatively high density of gas molecules, where they can collide with gas molecules and may

lose kinetic energy. These inelastic scattering events change the kinetic energy distribution of the outgoing electrons, resulting in a photoemission spectrum with additional background features.¹¹ While inelastic scattering in solids gives rise to relatively featureless background line shapes—that are often well approximated with the Tougaard universal cross section¹⁴—the narrow electronic states of molecules give rise to sharp features in the background line shape. For accurate analysis of sample properties, these features should be corrected for. This kind of correction is especially important when interpreting XPS spectra of broad asymmetric peaks containing complex satellite structures.

In a recent paper, we demonstrated that the electron transport theory implemented in the QUASES software¹⁵ can effectively be applied to remove these effects from the spectrum.¹⁶ In the present work, we use a similar approach and explore the fundamentals of the single and

This is an open access article under the terms of the Creative Commons Attribution License, which permits use, distribution and reproduction in any medium, provided the original work is properly cited.

© 2021 The Authors. *Surface and Interface Analysis* published by John Wiley & Sons Ltd.

multiple excitation processes in the gas molecules that are responsible for the inelastic background signal, and furthermore, we express the variation of the scattering properties of the gas directly by the gas pressure and temperature. Finally, we derive equations to simulate and remove signal due to inelastic scattering in the gas phase. We provide several examples where the equations have been applied, including gases He, O₂, H₂, and N₂ and materials Au, Ag, and Cu. As supporting information, we provide a python-based program that can be used to remove the background signal.¹⁷

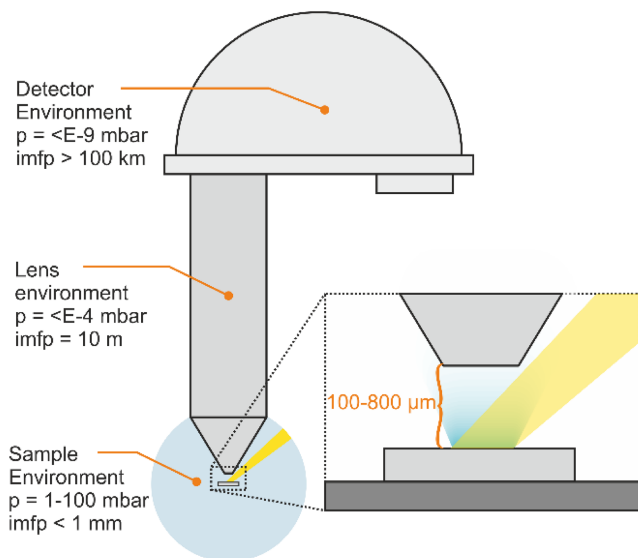


FIGURE 1 Schematic of a near-ambient pressure XPS set-up

2 | BACKGROUND

The theory needed to model how electron energy distributions change when passing through scattering media has been well established in fields of electron-energy loss spectroscopy (EELS)^{18–21} as well as in the photoemission community^{15,22–34} for modeling background signals in XPS spectra of solids and thin films. Here, we will derive the equations in the context of electron scattering in the gas phase and derive a relationship between electron energy distribution and gas pressure. Inelastic scattering in the gas phase has essentially the same effect as inelastic scattering through solid thin films, with the exception that, in the gas phase, interface effects and plasmon scattering do not play a role.

3 | SINGLE AND MULTIPLE ELECTRON SCATTERING AND CONVOLUTION

When an electron travels through a medium consisting of atoms, it can collide with these and transfer some of its kinetic energy to those atoms. In an electron-atom collision, the atoms can absorb energy in various ways, depending on the energy of the colliding electron. In electron spectroscopy, where photoelectrons have kinetic energies typically in the range of 100–2000 eV, the dominant channel for energy transfer is excitations from an occupied low-energy state to an unoccupied state at higher energy.

Figure 2 illustrates an example of how a population of electrons, with kinetic energy distribution shown in Figure 2A (red), responds after passing through a scattering medium consisting of hypothetical atoms, having only two states separated by the energy Δ , as shown in

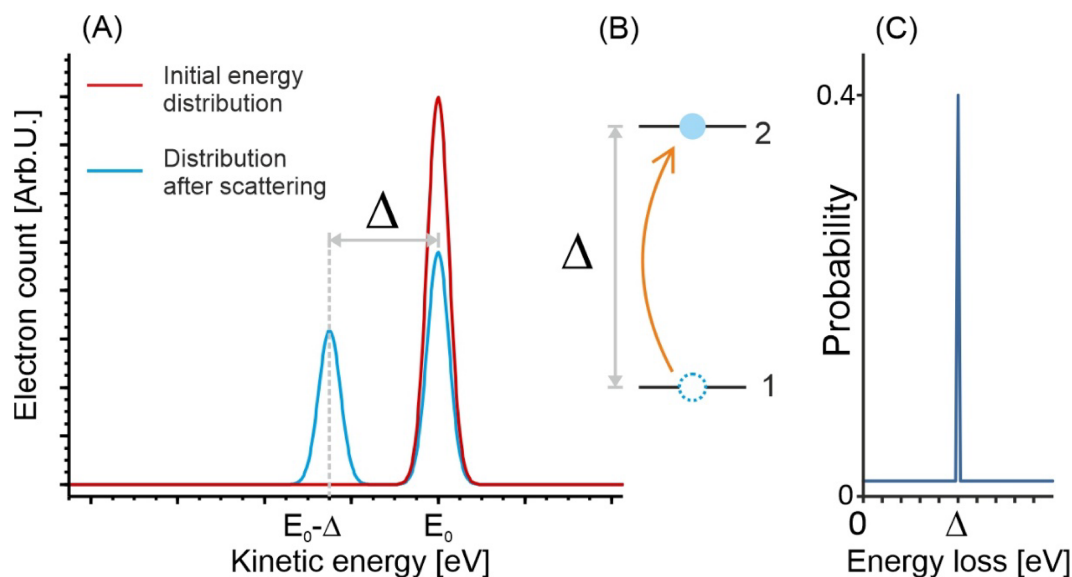


FIGURE 2 (A) Kinetic energy distribution of a hypothetical population of free-moving electrons. The red curve is the initial kinetic energy distribution. The blue curve is the distribution after having travelled through a hypothetical scattering medium. (B) The electronic structure of the hypothetical scattering medium, where the black lines represent electronic energy levels, the blue dot represents an electron, the dashed circle represents an electron-hole, and the orange arrow represents the process of electronic excitation. (C) The energy-loss probability function of the hypothetical scattering medium

Figure 2B. The incoming electrons have a narrow kinetic energy distribution centered around E_0 . When these electrons travel some path length through the scattering medium, there is a probability that any of these electrons will collide with an atom of the scattering medium and lose energy Δ to excite an electron in the atom to the higher energy state. The probability of transferring a given amount of energy in a collision is described by a probability distribution function, as illustrated in Figure 2C. Note that the probability distribution function in Figure 2C is closely related to various quantities discussed in the literature, such as imaginary part of the negative inverse of the dielectric function,³⁵ differential inelastic scattering cross section,³⁰ and differential inverse inelastic mean free path,²⁵ with subtle differences in meaning. In the present work, we will use the energy-loss function, which is the inelastic scattering cross section versus amount of energy lost.³⁵

The result of interacting with the scattering medium is that a fraction of the electrons (in this case 20%) lose energy Δ and now appear on the low kinetic energy side of E_0 as shown in Figure 2A (blue).

To generalize this model, the gas molecules may have several occupied and unoccupied electron states, and the loss function, which we will denote $L(\Delta)$, will have several peaks as shown in Figure 3B. These will all contribute to the possible energy loss processes, and the line shape of the scattered electron distribution can be constructed by taking the original unscattered electron distribution $F(E)$, scaling by the intensity of the energy-loss function at some point (Δ), then shifting the scaled spectrum by Δ . If one does this procedure, point-by-point, for all points on the energy-loss function, the sum will be the scattered line shape. This gives the energy distribution after scattering one time which we denote $I_1(E)$:

$$I_1(E) = \sum_{\Delta=0}^{\infty} F(E-\Delta)L(\Delta) \quad (1)$$

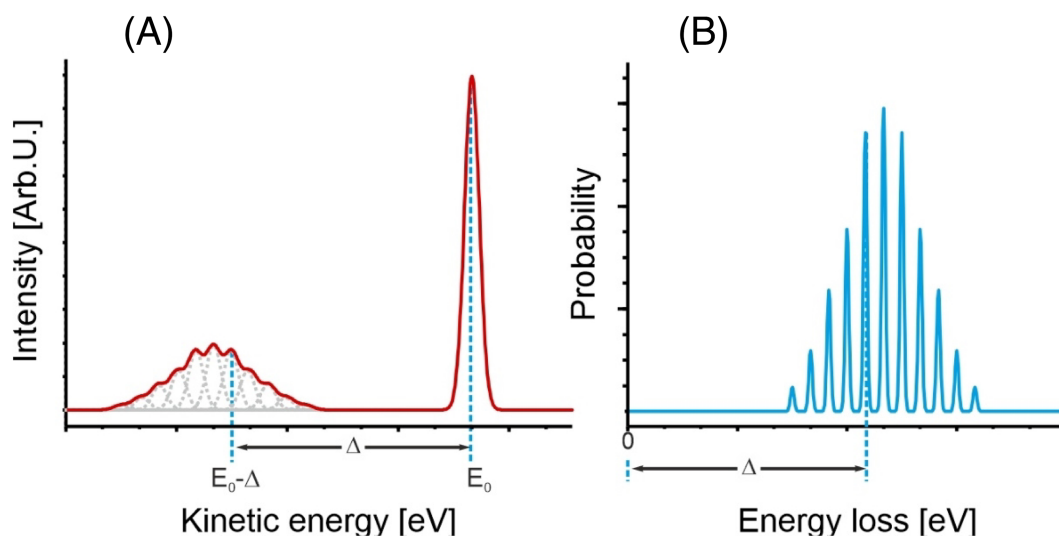


FIGURE 3 (A) Kinetic energy distribution of a hypothetical electron population after having been inelastically scattered by a scattering medium that has an energy-loss probability function shown in (B). The kinetic energy distribution of the electron population prior to scattering is Gaussian shaped and centered at E_0

which is the discrete form of a convolution:

$$F(x) \otimes L(x) = \int_0^x F(x-\Delta)L(\Delta)d\Delta \quad \text{for } F, L: [0, \infty) \quad (2)$$

In the preceding example, we made the implicit assumption that any given electron could only be scattered once when passing through the scattering medium. Of course, when passing through a medium of finite size, electrons may be scattered several times. The energy distribution of an electron population that has been scattered n times would simply be the line shape of the distribution after scattering $n - 1$ times, convolved once more with the energy-loss function. The result is equivalent to convolving the unscattered line shape with the energy-loss function n times:

$$I_0(E) = F(E) \quad (3)$$

$$I_1(E) = I_0(E) \otimes L(E) \quad (4)$$

$$I_2(E) = I_0(E) \otimes L(E) \otimes L(E) \quad (5)$$

$$I_3(x) = I_0(E) \otimes L(E) \otimes L(E) \otimes L(E) \quad (6)$$

The resulting line shapes of n convolutions between the primary distribution and the energy-loss function of Figure 3 are shown in Figure 4.

While the convolved line shapes provide the qualitative features in the resulting electron energy distribution, we need to know the probability that an electron is scattered n times when passing through the scattering medium, in order to determine how much each of the convolved line shapes contributes to the resulting distribution.

One can imagine an electron population passing through several infinitesimally thick layers of scattering medium, as depicted in Figure 5A. To be specific, we divide the total thickness t into d layers each of thickness t/d . The inelastic mean-free path (i.e., the mean distance between each inelastic scattering events) is denoted by λ . Then, for an infinitely small layer thickness t/d (i.e., for large d), the probability for an electron to be inelastically scattered once when passing through the layer of thickness t/d is $p_d = (t/d)/\lambda$ while the probability for multiple scattering in a single layer is negligible. The electron must pass through d layers, and the probability of being scattered n times is given by the binomial distribution:

$$P_n = \binom{d}{n} p_d^n (1-p_d)^{d-n} \quad (7)$$

$$\binom{d}{n} = \frac{d!}{n!(d-n)!} \quad (8)$$

Now $dp_d = t/\lambda$ and for d infinitely large, the binomial distribution converges to the Poisson distribution (using the Poisson Limit theorem)

$$\lim_{d \rightarrow \infty} \binom{d}{n} p_d^n (1-p_d)^{d-n} = \frac{\Lambda^n}{n!} e^{-\Lambda} \quad (9)$$

where the Poisson parameter $\Lambda = dp_d = \frac{t}{\lambda}$.

Thus, we have a formula to determine the probability of an electron being scattered n times when passing through a medium of thickness t :

$$P_n = \frac{1}{n!} \left(\frac{t}{\lambda}\right)^n e^{-t/\lambda} \quad (10)$$

With Equation 10, we can determine the scaling factors for the convolved line shapes and can now write a formula for the electron distribution after passing through the scattering medium:

$$J(E) = P_0 F(E) + P_1 F(E) \otimes L(E) + P_2 F(E) \otimes L(E) \otimes L(E) + \dots \quad (11)$$

where $J(E)$ is the measured electron distribution after passing through the scattering medium, $F(E)$ represents the initial electron energy distribution prior to any scattering, and $L(E)$ represents the energy loss function of the scattering medium.

An interesting and fortuitous property of convolution is that convolution in real space is equivalent to multiplication in Fourier space. This means that we can take the Fourier transform of Equation 11

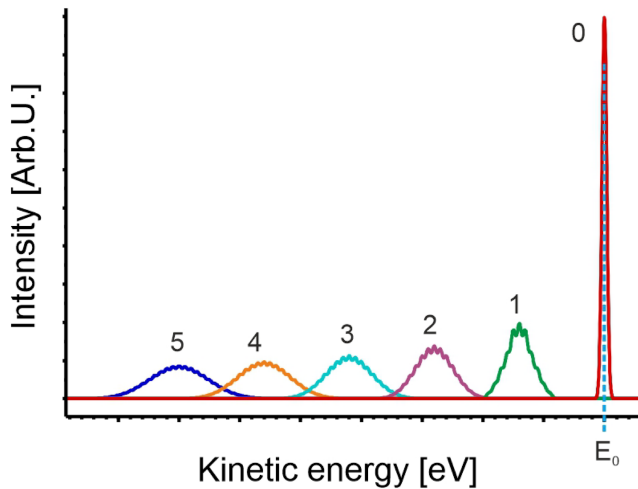


FIGURE 4 Kinetic energy distributions of a hypothetical electron population after having been scattered n times, by a hypothetical scattering medium with energy-loss function shown in Figure 3B. n are the numbers indicated in Figure 4

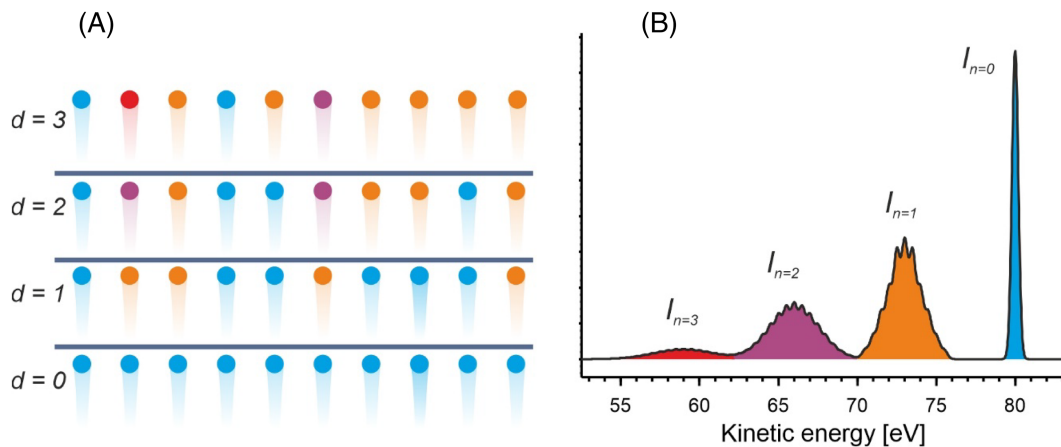


FIGURE 5 (A) Illustration of a mono-energetic population of electrons, passing through multiple infinitesimal planes of scattering medium. The electrons are represented by colored dots, where the color indicates the number of times having been inelastically scattered (blue:0, orange:1, purple:2, red:3). The probability of being inelastically scattered when passing through a plane of scattering medium is 0.4. (B) Hypothetical kinetic energy distribution of an electron population passing through four infinitesimal planes of scattering medium, where the probability of being inelastically scattered per plane is 0.4 and the energy-loss function is that shown in Figure 3B

and re-write it in terms of products instead of convolutions. Denoting $j(\nu)$, $f(\nu)$, and $l(\nu)$ to represent the Fourier transforms of $J(E)$, $F(E)$, and $L(E)$, respectively, we get

$$j(\nu) = P_0 f(\nu) + P_1 f(\nu)l(\nu) + P_2 f(\nu)l(\nu)^2 + \dots + P_n f(\nu)l(\nu)^n \quad (12)$$

$$j(\nu) = f(\nu) \left(P_0 + P_1 l(\nu) + P_2 l(\nu)^2 + \dots + P_n l(\nu)^n \right) \quad (13)$$

$$j(\nu) = f(\nu) \left(\frac{1}{0!} \left(\frac{t}{\lambda} \right)^0 e^{-t/\lambda} + \frac{1}{1!} \left(\frac{t}{\lambda} \right)^1 e^{-t/\lambda} l(\nu) + \dots + \frac{1}{n!} \left(\frac{t}{\lambda} \right)^n e^{-t/\lambda} l(\nu)^n \right) \quad (14)$$

Equation 14 is a Taylor series and can be re-written as

$$j(\nu) = e^{-t/\lambda} f(\nu) \exp\left(\frac{t}{\lambda} l(\nu)\right) \quad (15)$$

Thus, the measured electron energy distribution would be

$$J(E) = F^{-1} \left[e^{-t/\lambda} f(\nu) \exp\left(\frac{t}{\lambda} l(\nu)\right) \right] \quad (16)$$

where F^{-1} denotes the inverse Fourier transform.

In the context of electron scattering in a gas, we can rewrite Equation 16 as a function of gas pressure. Using the kinetic theory of gases, the mean free path can be written as

$$\lambda = \frac{1}{\sigma \rho} \quad (17)$$

where σ is the inelastic scattering cross section of the gas molecules and ρ is the volume density of the gas atoms. Using the ideal gas law, ρ can be re-written as

$$\rho = \frac{n}{V} = \frac{P}{RT} \quad (18)$$

and get

$$\lambda = \frac{RT}{\sigma P} \quad (19)$$

Now, our equation for the electron energy distribution becomes

$$J(E) = F^{-1} \left[e^{-t\sigma P/RT} f(\nu) \exp\left(\frac{t\sigma P}{RT} l(\nu)\right) \right] \quad (20)$$

Equation 20 gives a means to calculate the measured energy distribution, provided we know the primary energy distribution ($F(E)$), the energy-loss function ($L(E)$), the inelastic scattering cross section (σ) of the gas molecule, the pressure (P) and temperature (T) of the gas, and the distance (t) from the sample surface to the entrance of the

spectrometer. Alternatively, using this equation, one can remove the inelastic scattering background, given the energy-loss function, inelastic scattering cross section, and the experimental parameters P and t . This can be done using the Fourier-ratio de-convolution technique.^{18,20,36} From Equation 15, we obtain an expression for $f(\nu)$ and then we take the inverse Fourier transform to arrive at $F(E)$:

$$F(E) = F^{-1}(f(\nu)) = F^{-1} \left(j(\nu) e^{t/\lambda} \exp\left(\frac{-t}{\lambda} l(\nu)\right) \right) \quad (21)$$

4 | EXAMPLE OF ELECTRONS SCATTERED IN He

Using the model derived above, we will first consider the case of photoelectrons being scattered in Helium gas. Helium is an excellent example, as it is possibly the simplest scattering medium one can imagine. There are only two electrons on the atom, and no inter-atomic bonds, making its energy-loss spectrum rather simple.

Figure 6A shows a Au4f spectrum measured in ultra-high vacuum (red), a spectrum measured in 4 mbar He (blue), and a spectrum constructed by convolving, according to Equation 11, the spectrum measured in vacuum with the energy-loss function in Figure 6C, and scaling the convolved spectra by the probabilities calculated using Poisson statistics as given by Equation 10.

Comparing the spectrum taken in UHV with that in 4 mbar He, the intensity of the main XPS peak is seen to drop by about 25% due to scattering by the gas atoms. New features appear in the spectrum at around 1380 eV, as seen in Figure 6A. These features are the result of the primary electron distribution scattering one time by stimulating an electronic excitation in the He atoms. A closer look of the features caused by inelastic scattering is shown in Figure 6B. The two main features closely resemble the primary electron signal, but shifted to lower kinetic energy by 21.2 eV.

The loss function in Figure 6C, used to simulate the scattered signal, was determined by first constructing a synthetic spectrum qualitatively similar to published electron impact spectra of He.^{37,38} This was then optimized by using a stochastic pseudo-gradient descent algorithm to minimize the difference between the simulated and measured line shapes.³⁹ The resulting energy-loss function in Figure 6C can be easily interpreted, given helium's simple electron structure. The main peak at 21.2 eV corresponds to a $1s \rightarrow 2s$ transition, the second peak at approximately 23.1 eV to a $1s \rightarrow 2p$ transition, the third peak to several unresolved transitions $1s \rightarrow 3s, 3p, \dots 4f$ and the tail extending to much higher energies is due to ionization, that is, transitions from the $1s$ state into the continuum of unbound vacuum states.^{37,38}

The other parameters needed to simulate the scattered spectrum are the temperature and pressure of the gas (T , P), distance (t) between the sample and the first aperture of the spectrometer, and the inelastic scattering cross section (σ). The values of these parameters used to arrive at the fit shown in Figure 6 are $T = 298$ K, $P = 4$ mbar, and $t = 800$ μm while $\sigma = 0.0039$ nm^2 was determined by

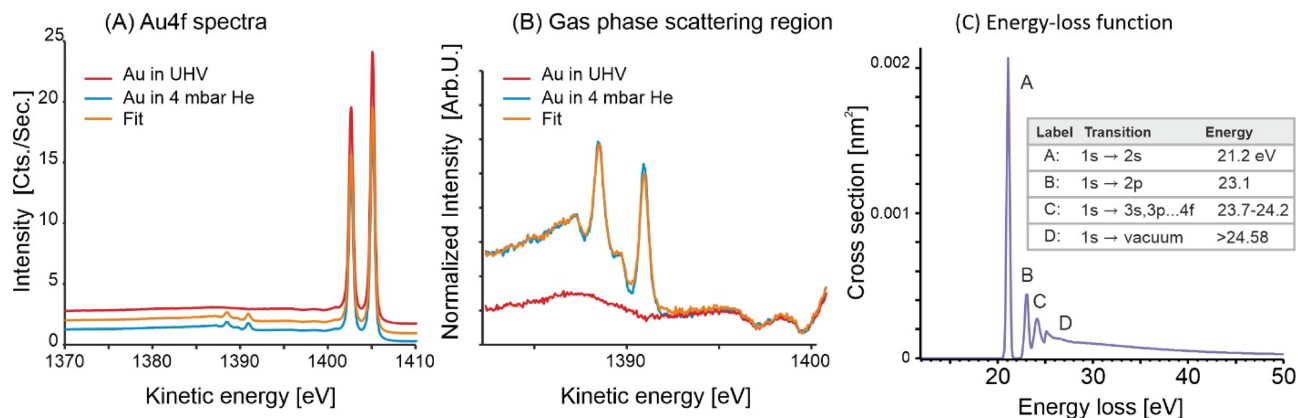


FIGURE 6 (A) Au4f XPS spectra measured in ultra-high vacuum (red), in 4 mbar He (blue) and the result of convolving the red spectrum with the energy-loss function of He, and scaling by the appropriate Poisson factor, as described in the derivation. (B) Detailed view of the spectra in A, focusing on the region where the inelastic scattering fine-structure appears. (C) Estimate of the energy-loss function of He. The inset indicates the electronic transition corresponding to each feature in the energy-loss function

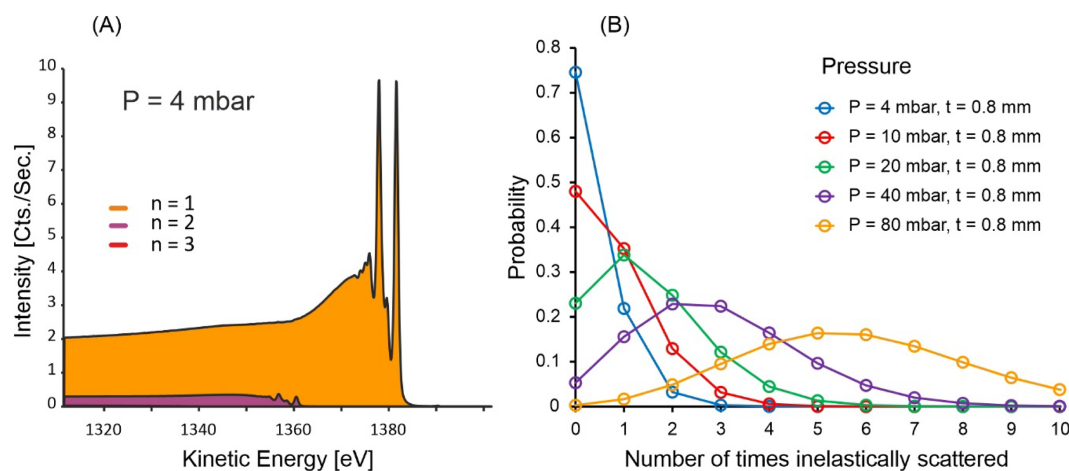


FIGURE 7 (A) The line shapes resulting from inelastic scattering, scaled by their respective Poisson factors, that were used to simulate the spectrum shown in Figure 6A. (B) Probabilities of inelastic scattering n times for electrons of kinetic energy 1380 eV, through 0.8 mm of gas phase He, at the pressures indicated

fitting the intensity at the peak energy. Once the energy-loss function and cross section are determined, spectra at other pressures can be simulated by simply changing P . In this case, we also measured at 2 mbar and could successfully reproduce the 2 mbar spectrum by changing P from 4 mbar to 2 mbar.

A plot of the contributions from single and multiple inelastic scattering is shown in Figure 7A. One can see that the main contributions is from electrons that have been inelastically scattered one time, with only a minor contribution from those that have been scattered twice. This is as expected because in 4 mbar He, the inelastic mean free path for electrons of 1400 eV kinetic energy is approximately 1.8 mm (using $\sigma = 0.0039 \text{ nm}^2$), and the distance traveled through the scattering medium in these measurements was 0.8 mm. Thus, plural scattering in this case is a rather rare event. Figure 7B shows the probabilities of scattering n -times for electrons of 1400 eV in various pressures of He, for a path length of 0.8 mm.

To verify that this approach can work at other pressures, we measured a spectrum at 25 mbar. To reach this pressure, we needed to change to a smaller first aperture (i.e., nozzle). The data at 4 mbar were measured with an 800- μm nozzle, at a sample distance of 800 μm , and the data at 25 mbar was measured using a 300- μm nozzle, and a sample distance of 300 μm . Thus, the parameters used to simulate the spectrum at 25 mbar were $T = 298 \text{ K}$, $P = 25 \text{ mbar}$, $t = 300 \mu\text{m}$, and $\sigma = 0.0039 \text{ nm}^2$. Note that the 300- μm distance gives rise to a different distribution between multiple scattering than shown in Figure 7B.

The measured and simulated spectra are shown in Figure 8. Here, one can see that at 25 mbar, plural scattering becomes significant. The feature arising from Au4f electrons being scattered twice in the gas phase can clearly be seen (the feature at kinetic energy $\sim 1360 \text{ eV}$). The perfect fit in the enlarged plot of the energy loss range in Figures 6B and 8B demonstrates that the convolution and

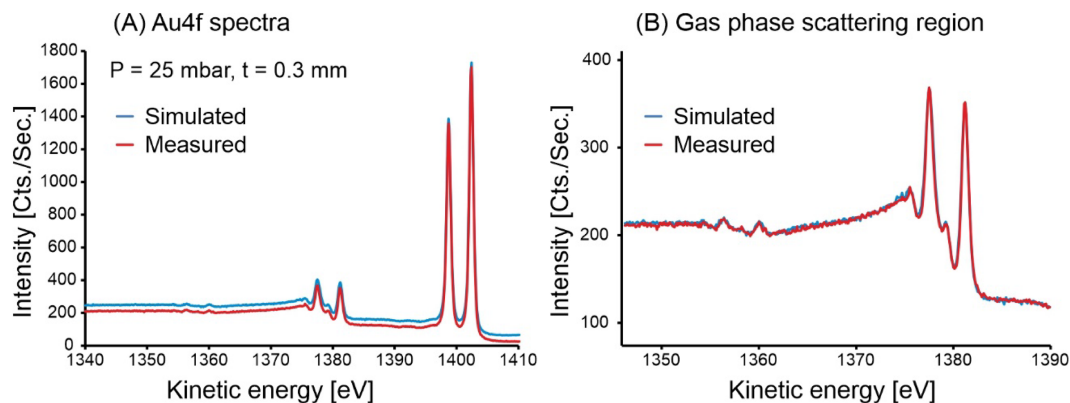


FIGURE 8 (A) Au4f XPS spectra of Au measured in 25 mbar He (red) and a spectrum simulated by convolving a reference spectrum measured in vacuum, with the energy-loss function of He, and scaling by the appropriate Poisson factors, as described in the derivations. (B) Enhanced view of the inelastic scattering region of the spectra in A

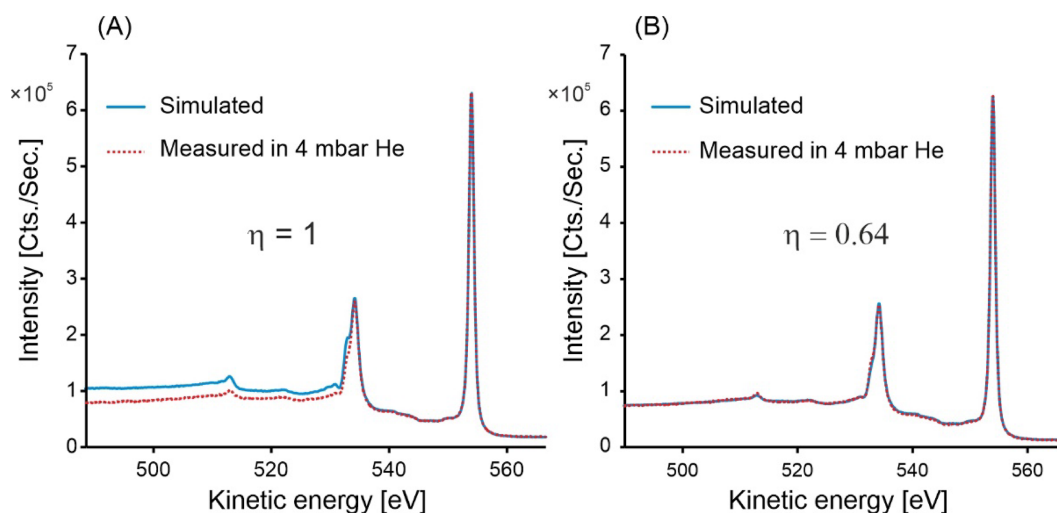


FIGURE 9 (A) Cu2p XPS spectrum measured in 4 mbar He (black dashed line) and simulated spectrum by convolving a spectrum measured in vacuum with the energy-loss function of He (orange). (B) Same spectra as in A, but a rescaling factor was used to construct the simulated spectrum (see details of the rescaling factor in main text)

scaling algorithm works very well even for substantially different pressures and measurement configurations. This gives confidence in the applied model.

The next test of the algorithm is to verify that it can work at other electron kinetic energies. To this end we measured a set of Cu2p spectra in He. With Al K- α as the excitation source, the kinetic energies of Cu2p_{3/2} and Au4f_{7/2} electrons are 554 and 1402 eV, respectively. This difference in kinetic energy should result in different inelastic scattering cross sections and could potentially influence the relative peak heights of the features in the loss function.

Figure 9A shows a Cu2p spectrum measured in 4 mbar He, as well as the simulated line shape, where the same loss function was used that was constructed using the Au4f data, and the only parameter change was the inelastic scattering cross section (0.0085 nm² at 530 eV for Cu2p and 0.0039 nm² at 1400 eV for Au4f). The intensity

of the main peak is fitted by choosing 0.0085 nm², but the intensities of the inelastically scattered features are too high. The reason why this occurs is that the loss function depends on the electron kinetic energy.

Let us conceptually divide the energy loss function into two parts: features from onsite excitations, that is, excitations between two states localized on an atom (such as peaks A, B, and C in Figure 6C) and features from ionization (i.e., feature D in Figure 6C). The onsite excitations give rise to the fine structure in the inelastically scattered spectrum, while ionization gives rise to the majority of intensity loss.⁴⁰ The line shape of the onsite excitation features varies little with the electron kinetic energy, for kinetic energies greater than ~ 100 eV. Thus, the line shape if this region of the loss function can be reused to fit spectra from wide range of kinetic energies. In contrast to onsite excitation, ionization does not strongly influence the line shape of the fine structure in the inelastically scattered spectrum. It does, however,

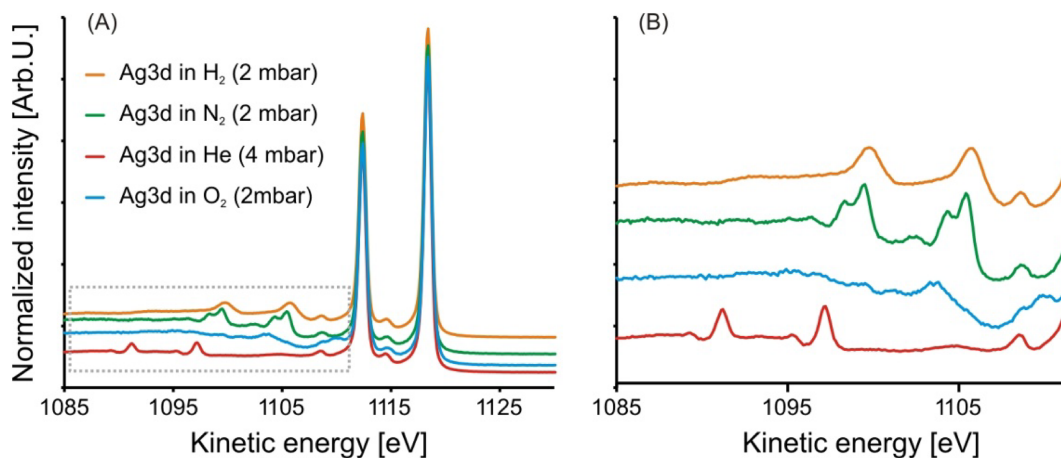


FIGURE 10 (A) Ag3d XPS spectra of Ag foil measured in various pressures of H₂, N₂, O₂, and He. (B) A detailed view of the gas phase inelastic scattering region from the spectra in A

strongly influence the overall intensity of the inelastically scattered signal.

Keep in mind that the total area under the energy-loss function is equal to the total inelastic scattering cross section. The ionization feature has a tail that extends hundreds of eV. The relative area of the ionization feature, compared with the onsite excitation features, depends on the kinetic energy of the colliding electron.^{40–43} So, while the line-shape resulting from the onsite excitations can be reused for many kinetic energies, the relative intensity of the ionization feature compared with the onsite features typically needs to be adjusted when changing kinetic energy.

Rather than re-fitting the loss function every time one changes kinetic energy, it is sufficient to include a rescaling factor. We have incorporated a rescaling factor into the algorithm to take care of this aspect. Our equation for the simulated spectrum Equation 20 then becomes

$$J(x) = F^{-1} \left[e^{-\eta \sigma P / RT} f(\nu) \exp \left(\frac{\eta \sigma P}{RT} I(\nu) \right) \right] \quad (22)$$

where the factor η accounts for the fact that not all of the primary signal intensity that was lost is accounted for by the modelled energy-loss function.

Figure 9B shows the measured and simulated Cu2p spectra with $\eta = 0.64$, and the fit is very good. The rescaling factor is more thoroughly explained in the supporting information, but effectively, it indicates what fraction of the total inelastic scattering cross section we were able to model with our synthetic energy-loss function.

5 | OTHER GASES (H₂, N₂, AND O₂)

While the case of inelastic scattering in He is an instructive example, it is seldom used in NAP-XPS experiments, so we have also investigated some more commonly used gases, namely, H₂, O₂ and N₂.

Figure 10 shows Ag4d XPS spectra measured in H₂, N₂, O₂, and He. It is seen that each gas results in a different fine structure in the inelastic scattering background signal. This observation is to be expected, given that each molecule has a distinct valence electronic structure.

The spectra with and without gas phase scattering were used to approximate the energy-loss function of each gas, as shown in Figure 11. To obtain these, we first estimated the energy loss functions from electron-impact spectra published in the 1960s.^{37,38,43–47} In doing so, we used a combination of Gaussian, Lorentzian, and the Universal Tougaard¹⁴ line shapes. These synthetic line shapes turned out to be very good estimates, and they were further refined using a stochastic pseudo-gradient descent algorithm to get the best fit of the simulated spectra to the experiment.

From the determined loss functions in Figure 11, we see that the molecules with higher number of valence electrons (i.e., N₂ and O₂) have rather complex energy-loss functions. Furthermore, diatomic molecules (i.e., H₂, N₂, and O₂) have vibrational fine structure that cannot be resolved in the line shapes shown here and appears in these line shapes as broadening. The vibrational fine structure can be seen in examples from previous literature of electron impact spectra.^{36,42}

The line shapes shown here were found to be relatively robust in the sense that they could be reused to simulate the gas-phase inelastic scattering signal for many photoemission spectra. To do that, one only needs to adjust the inelastic scattering cross section σ , and in some cases, the rescaling factor η , to accurately simulate the measured spectra. We measured several emission lines from Au, Cu, and Ag, in each of the gases H₂, He, N₂, and O₂ to obtain inelastic scattering cross sections for several electron kinetic energies. The measured emission lines were Cu2s, Cu2p, Ag3p, CuLMM, Au4p, Ag3d, Au4d, Au4f, Cu3p, and Au5d, having kinetic energies of 390, 555, 910, 920, 940, 1118, 1150, 1402, 1410, and 1480 eV, respectively. The spectra resulting from these measurements are available online. The resulting inelastic scattering cross sections are shown in Figure 12. One can see that the data points nicely fit to a power law, as expected from

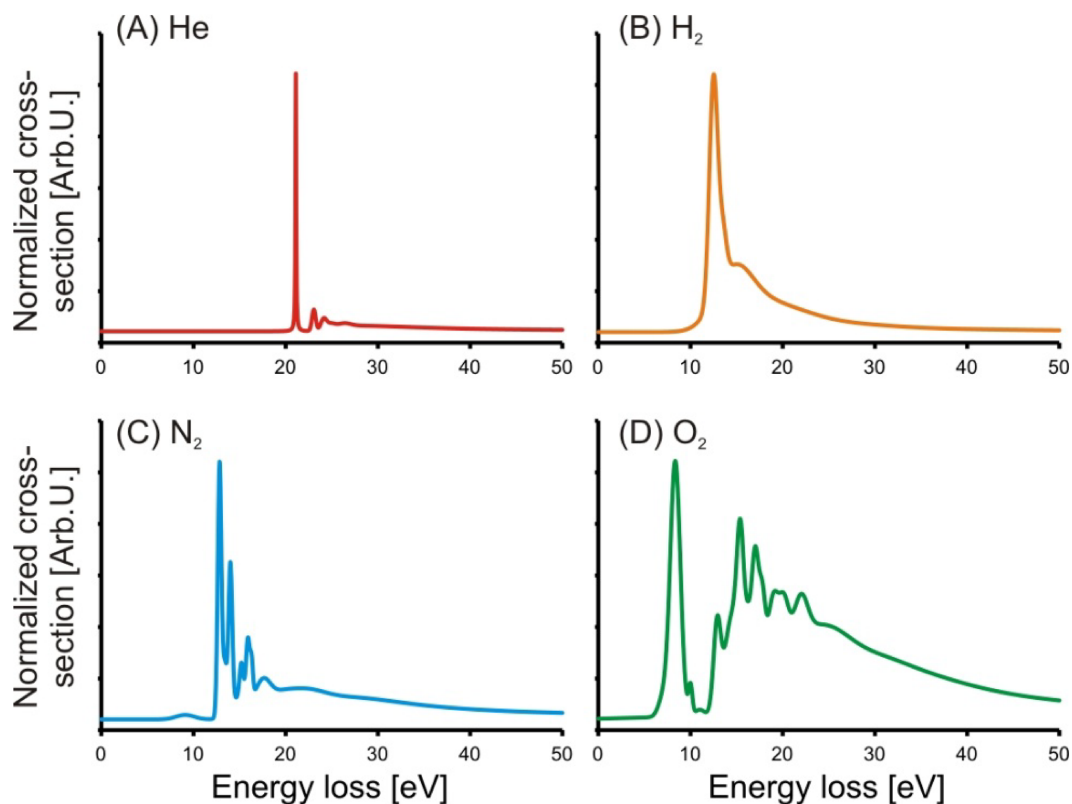


FIGURE 11 Energy-loss functions of the gases He (A), H₂ (B), N₂ (C), and O₂ (D) as determined from fitting the Ag3d spectra measured in the respective gas

previous works on scattering cross sections.⁴⁸ Note, in most literature about inelastic scattering of electrons in solids, plots like those in Figure 12 would typically show inelastic mean-free path (IMFP) versus energy. The metric of IMFP is useful in solids, where the density of the scattering medium does not vary significantly. In the gas phase, however, the density of the scattering medium changes with pressure and temperature. Thus, IMFP would be a function of pressure and temperature. Cross section, on the other hand, has particle density factored out, so that it does not depend on pressure and temperature.

In general, the workflow to determine the parameters for fitting/removing gas phase signal are as follows:

1. Measure a spectrum with and without gas phase present, keeping all instrument settings constant, and using a sample that will not change when exposed to the gas phase.
2. Use the algorithms set-out here and enter the known experimental parameters (i.e., pressure and distance) and use $\eta = 1$ for the rescaling factor.
3. Construct a trial energy-loss function and convolve the loss function with the spectrum measured in vacuum. Compare the resulting spectrum with the spectrum measured in gas.
4. Adjust the inelastic scattering cross section σ so the intensity of the main (i.e., zero-loss) peak of the simulated spectrum is the same as the intensity of the zero-loss peak of the spectrum measured in gas.

5. Optimize the loss function by tuning peak position, width and intensity, such that the most pronounced features of the spectrum measured in gas phase are reproduced.
6. If necessary, tune the scaling factor η to fit the intensity far away from the zero-loss peak.

Once this procedure has been completed, and the parameters have been determined for a given kinetic energy range, it can be used to remove the gas phase background signal for a real case, where the gas interacts with the surface atoms, although some fine tuning of parameters may still be warranted, depending on how well the parameters and loss function were optimized for the test spectra.

Here, we show an example of a spectrum measured in the presence of gas, where the features caused by inelastic scattering in the gas can be removed. Figure 13 shows Co2p spectra measured of Co₃O₄ while being heated in 1.8 mbar O₂, compared with a spectrum measured at room temperature in high vacuum and a spectrum simulated by deconvolving the spectrum measured in O₂ with the energy-loss function of O₂. One can see that the intensity around the satellite feature (i.e., at binding energy ~ 790 eV) decreases after removing the gas phase scattering signal. This kind of correction is especially important in cases where the chemical species are only stable in the presence of a reactive gas, and when the fine structure of features like satellites and multiplet is important for the chemical interpretation of the spectrum.

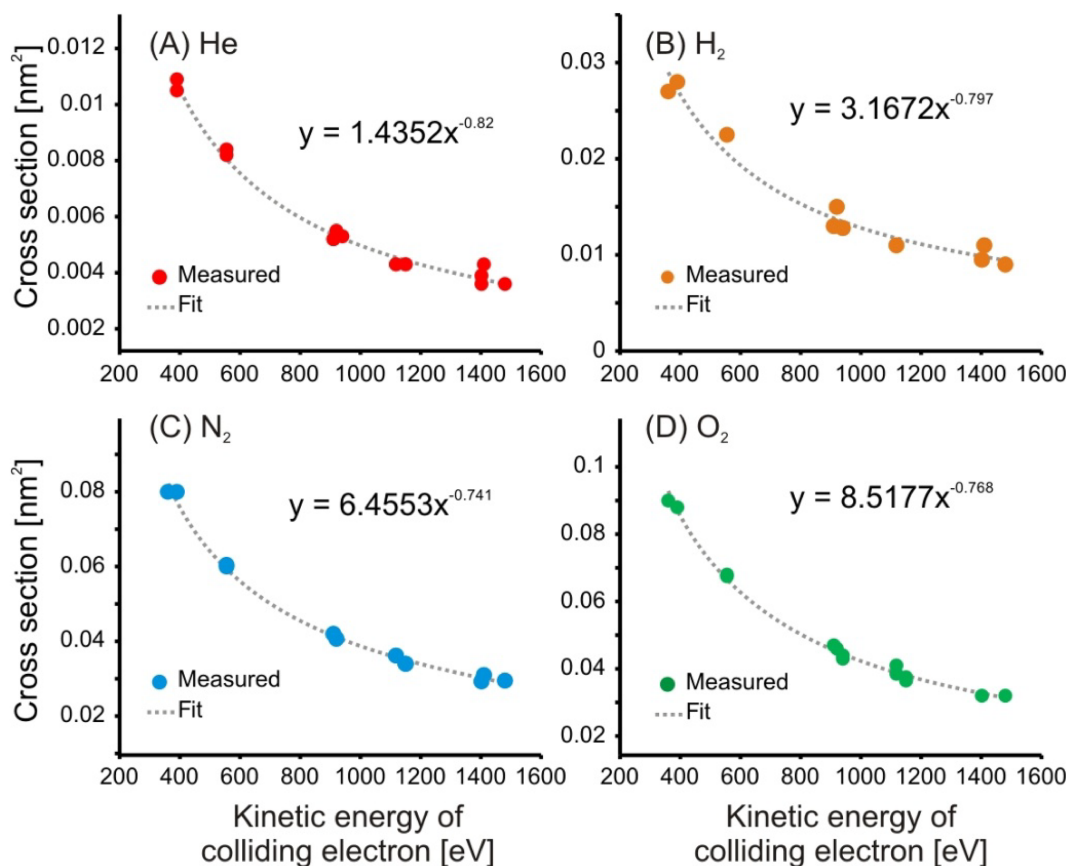


FIGURE 12 Inelastic scattering cross sections as a function of kinetic energy of the colliding electron for gases He (A), H₂ (B), N₂ (C), and O₂ (D). Measured values were determined by fitting the spectra measured in the presence of gas phase, with the spectrum measured in vacuum, after processing using the algorithm described in Equation 20 and optimizing the equations parameters. All spectra measured in the presence of gas were measured at pressures between 2 and 4 mbar, using an 800 μm diameter nozzle, with the samples placed at 800 μm away from the nozzle

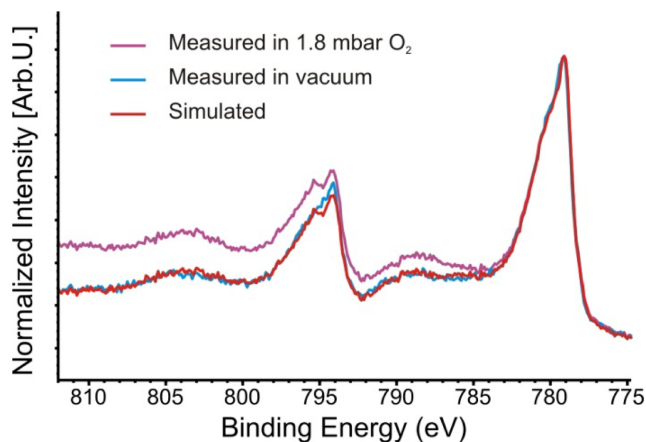


FIGURE 13 Co2p XPS spectra of Co₃O₄ measured in vacuum (blue), measured in 1.8 mbar O₂ (purple) and the simulated spectrum (red) resulting from deconvolving the spectrum measured in vacuum ($P < 1\text{E}-7$ mbar) with the O₂ energy-loss function, using Equation 21

6 | APPROXIMATIONS IN THE MODEL

It is important to understand the approximations made in the model shown here, so that one can understand the limits of applicability.

1 The model uses a single number for distance travelled through the scattering medium. Actually, electrons will travel a distribution of path lengths, depending on the size of the nozzle and its acceptance angle, as illustrated in Figure 14A. Here, L_{samp} is the distance between the sample and nozzle, D_{nozz} the nozzle diameter, D_{spot} the diameter of the illuminated spot on the sample, and θ the nozzle's acceptance angle. We see that an electron traveling at an angle of 0, relative to the nozzle axis, will travel a distance L_{samp} to the nozzle, while an electron traveling at an angle θ to the nozzle axis, will travel a distance $D_{\text{spot}}/\cos\theta$. Furthermore, the path length traveled by the electron can increase due to possible angular deflections. This effect turns out to be rather small and we found that it can be accurately corrected for by replacing the distance t by an average value L_{avg} which is slightly larger than L_{samp} (see Figure 15).

To evaluate the effect, we have used a Monte Carlo simulation to calculate the distribution of path lengths of electrons traveling through a gas phase, from a sample to a nozzle, where angular deflection was taken into account, as well as the change in scattering cross section as a function of kinetic energy. These calculations are published elsewhere.⁴⁹ Shown in Figure 14B are the results from a simulation of 2 million electrons, having initial kinetic energy of 1100 eV, traveling through 25 mbar of He, where the sample-nozzle distance

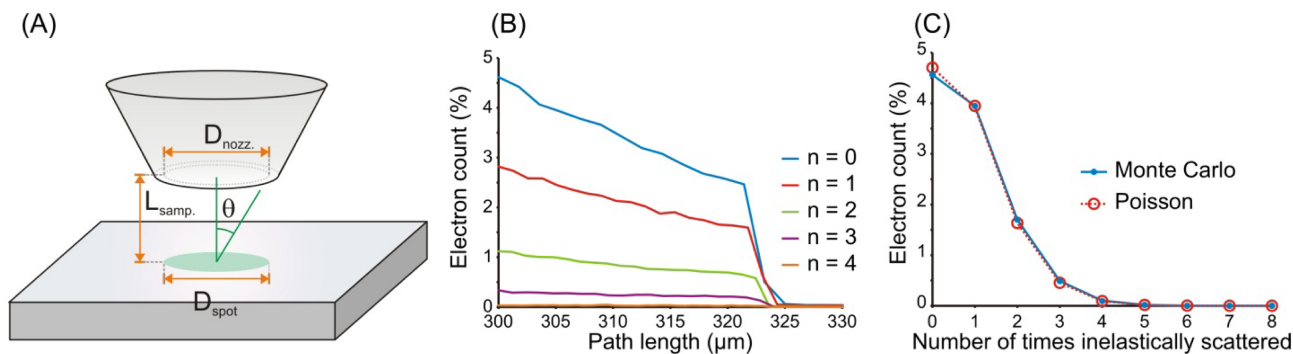


FIGURE 14 (A) Schematic representation of the sample-nozzle geometry, indicating the illuminated X-ray spot, with diameter D_{spot} , the nozzle diameter D_{nozz} , the sample-nozzle distance L_{samp} , and the acceptance angle θ . (B) Results of a Monte Carlo simulation of 2 million electrons, with initial kinetic energy 1100 eV, passing through He at 25 mbar, with a sample-nozzle distance of 0.3 mm, spot diameter of 0.3 mm, nozzle diameter of 0.3 mm, and acceptance angle 22° . This plot shows the electron count (as a percentage of the 2M electrons simulated) for only the electrons that intersected the nozzle at an angle of 22° , as a function of path length, for each of the n -times inelastically scattered. (C) A comparison of electron count versus number of times inelastically scattered as determined from the Monte Carlo simulation and the Poisson equation

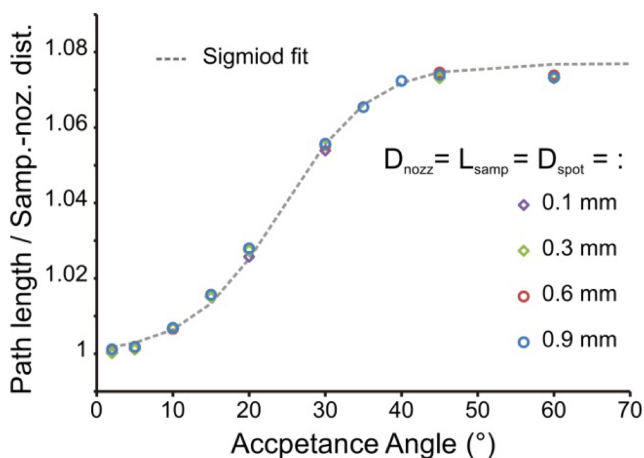


FIGURE 15 Plot of path length (t)/sample-nozzle distance (D_{samp}) as a function of acceptance angle, for cases where $D_{samp} = L_{samp} = D_{spot} = 0.1, 0.3, 0.6,$ and 0.9 mm. The results are from Monte Carlo simulations for 2 million electrons in 10 mbar He

was 0.3 mm, the nozzle diameter was 0.3 mm, the illumination spot diameter was 300 μm , and the acceptance angle was 22° (as is the case in our spectrometer). Here, we can see that the electrons that were not scattered ($n = 0$) exhibit path lengths between 0.3 and 0.325 mm. The sharp cut-off at path lengths greater than 0.325 mm is due to the acceptance angle. If we compare the results calculated from the Poisson equation, with results of the Monte Carlo simulate (Figure 14C), we see that a small error is introduced by ignoring the path length distribution and assuming that all electrons travelled the length L_{samp} . While, the deviation in the present case is small, it becomes larger as pressure increases and also depends on all other parameters shown in Figure 14A. We have found that using the average path length, from the distribution shown in Figure 14B, one can very effectively correct for the error. However, the average path length depends on L_{samp} , D_{spot} , D_{nozz} , and θ . If one sets

$L_{samp} = D_{spot} = D_{nozz}$, as is usually the case in NAP-XPS experiments, then one can estimate the average path length as a function of acceptance angle, using an empirical fit to the Monte Carlo simulations. We have found that the average path length divided by sample-nozzle distance, can be fit well with a sigmoid function of the form $L_{avg} \sim 1 + 0.077 / (1 + \exp(0.168(24.3 - x)))$, as shown in Figure 15. In the case of $\theta = 22^\circ$, the average path length is 3% larger than the sample-nozzle distance. Thus, the value for t that should be used in Equation 22 for this case, should be $1.03 \times L_{samp}$.

- The model uses a constant inelastic scattering cross section. In principle, the inelastic scattering cross section is a function of kinetic energy and will change as the electrons experience more scattering and lose kinetic energy. However, over the kinetic energy ranges that are typical for a detailed XPS spectrum, the change in cross section is negligible.
- In the model, we assume that the energy-loss function is independent of kinetic energy. In reality, the relative intensity of the features in the loss function depends on the kinetic energy of the colliding electrons. For instance, at very low kinetic energies, the intensity ratios of the peaks in the loss function can change significantly with kinetic energy.¹⁰ For kinetic energies above 100 eV, however, the peak ratios remain nearly constant.
- This model treats the gas phase as though its pressure is constant from the sample to the nozzle, and zero after the nozzle. Fluid flow calculations⁵⁰ show that, close to the nozzle, the pressures deviate from this approximation. However, due to symmetry, the pressure drop on the high-pressure side is counteracted by the pressure increase on the vacuum side, such that the integral of distance and density is the same as the case where there is an abrupt drop in pressure across the nozzle. The situation where this would not be the case is when very high gas pressures are used, such that a jet forms inside the vacuum side. Such situations are not covered by this model.

5 In addition to inelastic scattering, electrons can also be elastically scattered by gas molecules along their path to the nozzle. When an electron collides elastically with an atom, it can change its direction of travel. While this is also true for inelastic scattering, the angular deflection upon elastic scattering is much more substantial than for inelastic scattering. As a consequence of the deflection, an electron that may have initially had a trajectory that would lead it into the nozzle, might, after collision, be deflected away from the nozzle. Consequently, elastic scattering gives rise to a loss in total signal. The precise amount of signal lost is a function of gas pressure, differential elastic scattering cross section, sample-nozzle distance, acceptance angle, X-ray spot size, and nozzle diameter, and is not trivial to calculate.

However, under the conditions one would typically use for NAP-XPS measurements, that is, under circumstances where scattering in the gas phase is minimized to the point where one can still obtain a useful XPS spectrum, the signal loss due to elastic scattering is quite low. For instance, using a sample-nozzle distance, X-ray spot diameter and nozzle diameter of 0.5 mm, in 5 mbar of He, the amount of signal lost due to elastic scattering would be 0.3%. In contrast, using the same configuration, but with a pressure of 30 mbar, the signal lost due to elastic scattering would be approximately 2%. These numbers were obtained using Monte Carlo simulations and are described in more detail in the supporting information. In general, most NAP-XPS measurements would be performed under circumstances where losses from elastic scattering would be negligible.

7 | EXPERIMENTAL

All spectra presented in this work were measured using a Phoibos NAP-150 hemispherical analyzer from Specs GmbH. The nozzle used to separate the sample environment from the electrostatic lens system had a diameter of 0.8 mm in cases where the pressure was <5 mbar, and 0.3 mm in cases where the pressure was >5 mbar. The distance from the sample surface to the entrance aperture of the nozzle was always set to be equal to the nozzle diameter. Samples were sputter cleaned using argon ions (at 3 kV, a pressure of 1×10^{-5} mbar, and an emission current of 10 mA, for 15 min), to remove adventitious carbon and any surface oxides. During XPS measurements where gas phase was present, gas was leaked into the sample chamber using a mass flow controller, and pressure was held constant during measurement by means of a throttle valve. The throttle valve controls the pumping cross section of a differential pumping stage. Pressure was measured using a diaphragm capacitance pressure.

ACKNOWLEDGEMENT

Open Access funding enabled and organized by Projekt DEAL.

ORCID

Lukas Pielsticker  <https://orcid.org/0000-0001-9361-8333>

Sven Tougaard  <https://orcid.org/0000-0003-0909-8764>

Mark Greiner  <https://orcid.org/0000-0002-4363-7189>

REFERENCES

1. Zhong L, Chen D, Zafeiratos S. A mini review of in situ near-ambient pressure XPS studies on non-noble, late transition metal catalysts. *Cat Sci Technol*. 2019;9(15):3851-3867.
2. Trotochaud L, Head AR, Karslıoğlu O, Kyhl L, Bluhm H. Ambient pressure photoelectron spectroscopy: practical considerations and experimental frontiers. *J Phys Condens Matter*. 2016;29(5):053002.
3. Salmeron M, Schlögl R. Ambient pressure photoelectron spectroscopy: a new tool for surface science and nanotechnology. *Surf Sci Rep*. 2008;63(4):169-199.
4. Arble C, Jia M, Newberg JT. Lab-based ambient pressure X-ray photoelectron spectroscopy from past to present. *Surf Sci Rep*. 2018;73(2):37-57.
5. Kaya S, Ogasawara H, Näslund L, et al. Ambient-pressure photoelectron spectroscopy for heterogeneous catalysis and electrochemistry. *Catal Today*. 2013;205:101-105.
6. Salmeron M. From surfaces to interfaces: ambient pressure XPS and beyond. *Top Catal*. 2018;61(20):2044-2051.
7. Chang R, Hong YP, Axnanda S, et al. In-situ photoelectron spectroscopy with online activity measurement for catalysis research. *Curr Appl Phys*. 2012;12(5):1292-1296.
8. Starr D, Liu Z, Hävecker M, Knop-Gericke A, Bluhm A. Investigation of solid/vapor interfaces using ambient pressure X-ray photoelectron spectroscopy. *Chem Soc Rev*. 2013;42(13):5833-5857.
9. Crumlin E, Bluhm H, Liu Z. In situ investigation of electrochemical devices using ambient pressure photoelectron spectroscopy. *J Electron Spectrosc Relat Phenom*. 2013;190:84-92.
10. Palomino R, Hamlyn R, Liu Z, et al. Interfaces in heterogeneous catalytic reactions: ambient pressure XPS as a tool to unravel surface chemistry. *J Electron Spectrosc Relat Phenom*. 2017;221:28-43.
11. Jürgensen A, Esser N, Hergenröder R. Near ambient pressure XPS with a conventional X-ray source. *Surf Interface Anal*. 2012;44(8):1100-1103.
12. Maibach J, Xu C, Eriksson S, et al. A high pressure x-ray photoelectron spectroscopy experimental method for characterization of solid-liquid interfaces demonstrated with a Li-ion battery system. *Rev Sci Instrum*. 2015;86(4):044101.
13. Filippetti A, Fiorentini V. Magnetic ordering in CuO from first principles: a cuprate antiferromagnet with fully three-dimensional exchange interactions. *Phys Rev Lett*. 2005;95(8):086405.
14. Tougaard S. Universality classes of inelastic electron scattering cross-sections. *Surf Interface Anal*. 1997;25(3):137-154.
15. Tougaard S. Software packages to characterize surface nanostructures by analysis of electron spectra. QUASES.com, 2020. Available: <http://www.quases.com/products/quases-tougaard/>
16. Tougaard S, Greiner M. Method to correct ambient pressure XPS for the distortion caused by the gas. *Appl Surf Sci*. 2020;530:147243.
17. Greiner M, Pielsticker L, Nicholls R. surfaceanalytics/inelasticscattering: Initial release. 2021. <https://doi.org/10.5281/zenodo.4572457>
18. Wang F, Egerton R, Malac M. Fourier-ratio deconvolution techniques for electron energy-loss spectroscopy (EELS). *Ultramicroscopy*. 2009;109(10):1245-1249.
19. Egerton R. Electron energy-loss spectroscopy in the TEM. *Rep Prog Phys*. 2008;72(1):016502.

20. Egerton R, Williams B, Sparrow T. Fourier deconvolution of electron energy-loss spectra. *Proc R Soc Lond a Math Phys Sci.* 1985;398(1815):395-404.
21. Johnson D, Spence J. Determination of the single-scattering probability distribution from plural-scattering data. *J Phys D Appl Phys.* 1974;7(6):771-780.
22. Yubero F, Sanz JM, Ramskov B, Tougaard S. Model for quantitative analysis of reflection electron energy loss spectra: angular dependence. *Phys Rev B.* 1996;53(15):9719-9727.
23. Werner W. Differential surface and volume excitation probability of medium-energy electrons in solids. *Phys Rev B.* 2006;74(7):075421.
24. Werner W. Electron transport for spectrum analysis and experiment design. *J Electron Spectrosc Relat Phenom.* 2010;178-179:154-177.
25. Werner W. Simulation of electron spectra for surface analysis using the partial-intensity approach (PIA). *Surf Interface Anal.* 2005;37(11):846-860.
26. Werner W. Trajectory reversal approach for electron backscattering from solid surfaces. *Phys Rev B.* 2005;71(11):115415.
27. Werner W, Cabela T, Zemek J, Jiricek P. On line shape analysis in X-ray photoelectron spectroscopy. *Surf Sci.* 2001;470(3):325-336.
28. Pauly N, Yubero F, Tougaard S. Quantitative analysis of satellite structures in XPS spectra of gold and silver. *Appl Surf Sci.* 2016;383:317-323.
29. Tougaard S. Energy loss in XPS: fundamental processes and applications for quantification, non-destructive depth profiling and 3D imaging. *J Electron Spectrosc Relat Phenom.* 2010;178-179:128-153.
30. Tougaard S, Chorkendorff I. Differential inelastic electron scattering cross sections from experimental reflection electron-energy-loss spectra: application to background removal in electron spectroscopy. *Phys Rev B.* 1987;35(13):6570-6577.
31. Tougaard S, Kraaer J. Inelastic-electron-scattering cross sections for Si, Cu, Ag, Au, Ti, Fe, and Pd. *Phys Rev B.* 1991;43(2):1651-1661.
32. Smekal W, Werner W, Powell C. Simulation of electron spectra for surface analysis (SESSA): a novel software tool for quantitative Auger-electron spectroscopy and X-ray photoelectron spectroscopy. *Surf Interface Anal.* 2005;37(11):1059-1067.
33. Cohen Simonsen A, Yubero F, Tougaard S. Quantitative Model for Electron Energy Loss in XPS. *Phys Rev B.* 1997;56(3):1612-1619.
34. Pauly N, Tougaard S, Yubero F. Determination of the Cu 2p primary excitation spectra for Cu, Cu₂O and CuO. *Surf Sci.* 2014;620:17-22.
35. Nguyen-Truong HT. Energy-loss function including damping and prediction of plasmon lifetime. *J Electron Spectrosc Relat Phenom.* 2014;193:79-85.
36. Cheng SC, Wang YY, Dravid VP. The intensity of elastic and inelastic multiple scattering in EELS. *Micron.* 1996;27(2):167-170.
37. Skerbele A, Lassetre E. Higher-resolution study of the electron-impact spectrum of helium. *J Chem Phys.* 1964;40(5):1271-1275.
38. Lassetre E. Inelastic scattering of high energy electrons by atmospheric gases. *Can J Chem.* 1969;47(10):1733-1774.
39. Yenice Z, Adhikari N, Wong Y, Aksakalli V, Gumus A, Abbasi B. SPSA-FSR: simultaneous perturbation stochastic approximation for feature selection and ranking. *arXiv preprint arXiv:1804.05589*, 2018.
40. Itikawa Y. Cross sections for electron collisions with oxygen molecules. *J Phys Chem Ref Data Monogr.* 2009;38(1):1-20.
41. Itikawa Y. Cross sections for electron collisions with nitrogen molecules. *J Phys Chem Ref Data Monogr.* 2006;35(1):31-53.
42. Yoon J-S, Song M-Y, Han J-M, et al. Cross sections for electron collisions with hydrogen molecules. *J Phys Chem Ref Data Monogr.* 2008;37(2):913-931.
43. Lassetre E, Skerbele A, Dillon M, Ros K. High-resolution study of electron-impact spectra at kinetic energies between 33 and 100 eV and scattering angles to 16°. *J Chem Phys.* 1968;48(11):5066-5096.
44. Lassetre E, Krasnow M, Silverman S. Inelastic scattering of electrons by helium. *J Chem Phys.* 1964;40(5):1242-1248.
45. Lassetre E, Krasnow M. Collision cross-section study of two transitions in nitrogen. *J Chem Phys.* 1964;40(5):1248-1255.
46. Lassetre E, Francis S. Inelastic scattering of 390-V electrons by helium, hydrogen, methane, ethane, cyclohexane, ethylene, and water. *J Chem Phys.* 1964;40(5):1208-1217.
47. Lassetre E, Silverman S, Krasnow M. Electronic collision cross sections and oscillator strengths for oxygen in the Schumann-runge region. *J Chem Phys.* 1964;40(5):1261-1265.
48. Shinotsuka H, Tanuma S, Powell C, Penn D. Calculations of electron inelastic mean free paths. X. Data for 41 elemental solids over the 50 eV to 200 keV range with the relativistic full Penn algorithm. *Surf Interface Anal.* 2015;47(9):871-888.
49. Pielsticker L, Schlögl R, Greiner M. Monte Carlo calculations for simulating electron scattering in gas phase. *ArXiv preprint arXiv:2101.01561*, 2021.
50. Karslıoğlu O, Bluhm H. Ambient pressure X-ray photoelectron spectroscopy. In: *Operando Research in Heterogeneous Catalysis*. Springer; 2017.

SUPPORTING INFORMATION

Additional supporting information may be found online in the Supporting Information section at the end of this article.

How to cite this article: Pielsticker L, Nicholls R, Beeg S, et al. Inelastic electron scattering by the gas phase in near ambient pressure XPS measurements. *Surf Interface Anal.* 2021;53:605-617. <https://doi.org/10.1002/sia.6947>